Adaptive Virtual Resistance for Postfault Oscillation Damping in Grid-Forming Inverters

Me, Si Phu; Zabihi, Sasan; Blaabjerg, Frede; Bahrani, Behrooz

Adaptive Virtual Resistance for Post-fault Oscillation Damping in Grid-forming Inverters

Si Phu Me, *Student Member, IEEE*, Sasan Zabihi, *Senior Member, IEEE*,
Frede Blaabjerg, *Fellow, IEEE*, and Behrooz Bahrani, *Senior Member, IEEE*

Abstract—Post-fault oscillations in active power and voltage responses of grid-connected Voltage Source inverters (VSIs) have been reported in the literature. They are caused by non-ideally-tuned controllers and the implemented current limitations used for protecting the VSIs from over-currents. These oscillations become even more significant when the VSI is connected to a weak grid, deteriorating the recovery process of the VSI. This paper presents a method for damping the post-fault oscillations by using an adaptive virtual resistor (VR). Even though these oscillations are observed with both grid-following and grid forming inverters, this paper focuses on droop-based grid-forming inverters. The proposed method dynamically integrates a VR into the VSI control and removes it in the normal operation mode of the VSI. This method is implemented in the Synchronous Reference Frame (SRF), which is commonly used due to its decoupled active and reactive power control. The amount of virtual resistance used for oscillation damping is adaptive to the recovery rate of the VSI. Hence, the proposed method is robust against changes in grid strength. Finally, the performance of the method is evaluated in PSCAD/EMTDC and also experimentally validated.

Index Terms—Current Limitation, Grid-forming Inverter, Virtual Impedance, Voltage Source Converters.

I. INTRODUCTION

GRID-forming inverters (GFMIs) have been attracting significant attention in the literature due to their flexibility in both grid-connected and standalone operation [1], and being able to overcome the drawbacks of the grid-following inverters [2]–[4]. Various grid-forming control structures for GFMIs have been proposed, including droop-based control [5], [6], virtual synchronous generator (VSG) control [7], [8], synchronous power control (SPC) [1], power synchronization control [9], and virtual oscillator control [10]. Among them, droop control and VSG are the most widely used structures [11], [12].

Due to the low over-current capability of the semiconductor switches inside the GFMIs, a current limitation is employed to limit the over-current and protect the switches during voltage sag events. Without over-sizing, the over-current limit is usually set between 1.1 per unit (pu) and 1.4 pu [13]. However, the inverter current limitation might result in poor post-fault transient [14], [15]. Besides, improperly-tuned controllers of GFMIs and/or their supporting equipment, e.g., synchronous condenser, can lead to oscillatory transients and overshoots in post-fault responses [16]. Moreover, the oscillatory transients in voltage

and power responses become more significant as the grid gets weaker [1], [16]. Hence, a damping mechanism is necessary to suppress such oscillations. Virtual impedance (VI) can be used for this purpose [1].

VI has been widely used in voltage source inverters (VSIs) for various purposes, including reactive power sharing enhancement [17], current limitation [13], small-signal stability improvement [18], and transient damping [1], [19]–[21]. However, transient damping is the only focus in this paper. Ref. [19] mainly focuses on the stability enhancement obtained by using VI for current limiting in load change events. High-pass filters are used for transient enhancement in [19]. However, the impacts of the high-pass filters and post-fault transient suppression are not studied in this reference. The proposed method in [20] shows improvements in oscillation elimination in line trip events, but no study on post-fault oscillations is conducted in this work. In [21], parallel virtual resistors (VRs) are integrated into standalone VSIs for suppressing post-fault over-voltage. This approach is implemented in a natural reference frame, which requires independent control for each phase, leading to a higher level of control complexity. Moreover, switching to a current-controlled mode, as implemented in [21], might cause problems relating to the phase-locked loop's (PLL) stability and a reduction in the critical clearing angle [3], [4], [22]. In [1], a VR model, which is temporarily integrated into the control when a fault recovery is detected, is proposed. It can mitigate the post-fault oscillations without impacting the normal operation of the VSI. The proposed VR in [1] is implemented in SPC, and no design guidelines are explicitly given for the VR. In addition, the impact of different grid strength conditions on the performance of the VR is totally disregarded in [1].

The grid strength is typically defined by the short circuit ratio (SCR) [3]. The SCR reduces when the line impedance increases. As a result, the sensitivity between changes in voltage and changes in current and power is higher. During a fault recovery in a low-SCR network, large changes in the voltage magnitude at the point of common coupling (PCC) and its angle can cause higher deviations in the power and the current, hence higher-magnitude oscillations [1], [16]. Therefore, post-fault oscillation magnitude depends on the grid strength of the connected grid. In stiffer grids, the oscillation's magnitude is not excessively high. Therefore, a lower amount of virtual resistance damping is required, compared to weak grid conditions. This paper aims at studying the effects of the VR used for oscillation damping in the fault recovery process of droop-based GFMIs. The study reveals that, along with the current saturation used for over-current protection, excessive virtual resistance can result in a slow recovery process or even instability, especially when the GFMI is connected to a stiff grid. To address this problem, an adaptive VR (AVR) model based on the rate of power recovery
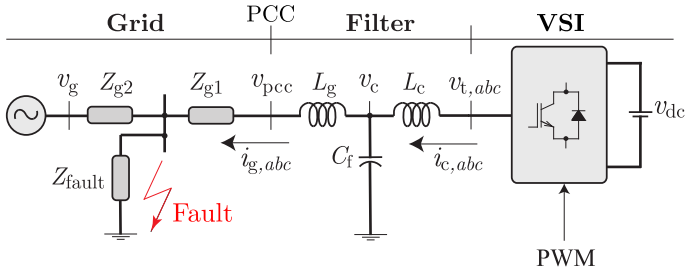
Fig. 1. A grid-connected VSI with a symmetrical fault.

is then proposed. The AVR model can self-adjust the amount of virtual resistance such that the post-fault oscillation is sufficiently dampened without resisting the recovery process unnecessarily.

This paper is structured as follows. The system overview and the post-fault oscillation problem are given in Section II. In Section III, a stability study of the GFMI with the presence of the fixed-value VR and current limitation is provided, followed by an adaptive VR proposal. Simulation and experimental validation of the findings are presented in Section IV. Finally, the conclusions of the paper are summarized in Section V.

II. POST-FAULT OSCILLATION

In this section, first, an overview of the GFMI's control system is described. Then, a study on the post-fault oscillation phenomenon is presented.

A. Configuration of a Cascade GFMI

As shown in Fig. 1, a three-phase VSI is connected to the grid via an LCL filter, consisting of L_c, C_f, and L_g. The grid is modelled as an ideal AC voltage source connected in series with the line impedance segmented into two parts, i.e., Z_{g_1} and Z_{g_2}. v_g, v_{pcc}, v_c, and $v_{t,abc}$ are the output voltage of the ideal AC source, the voltage at the PCC, the capacitor voltage, and the terminal voltage of the VSI, respectively, while $i_{c,abc}$ and $i_{g,abc}$ represent the inverter-side and the grid-side currents, respectively. In Fig. 2, the control structure of the VSI is depicted as three cascade loops implemented in a Synchronous Reference Frame (SRF). Vector control is applied to voltage and current control of the VSI to form the two inner control loops. More details on tuning these control loops can be found in [6], [23], [24]. The direct voltage reference, $v_{d,ref}$, is provided by the Q-V droop in the primary control loop, while the quadrature counterpart, $v_{q,ref}$, is set to zero to align $v_{d,ref}$ with the capacitor voltage vector. The primary control also consists of a P-f droop to help synchronize the VSI with the grid and regulate the active power transfer between them. In addition, a low-pass filter (LPF) is added to the P-f droop and the Q-V droop for filtering the measurement noise in the power. Moreover, to enable the virtual inertia provision of the P-f droop, and to make the P-f droop equivalent to the swing equation of a synchronous generator, the LPF is applied to the active power error in this control loop [25], [26]. The droop controls are governed by

$$\omega_{vsi} - \omega_0 = K_P \frac{\omega_{pc}}{s + \omega_{pc}}(P^* - P_m) \qquad (1)$$

and

$$v_{d,ref} - V_0 = K_Q(Q^* - \frac{\omega_{qc}}{s + \omega_{qc}}Q_m), \qquad (2)$$

where ω_{vsi}, ω_0, P^*, and P_m are the internal angular frequency of the VSI, the nominal frequency of the grid in pu, the active power reference, and the measured active power, respectively. V_0, Q^*, and Q_m denote the nominal line-to-line RMS voltage at the PCC, the reactive power reference and the measured reactive power of the VSI, respectively. Moreover, K_P is the P-f droop gain while K_Q is the counterpart for the Q-V droop. Finally, ω_{pc} and ω_{qc} are the cut-off frequencies of the low-pass filters [25].

B. Current Saturation and Power Adjustment

To protect the semiconductor switches inside the GFMI in voltage sag events, the output current must be kept below a maximum value, i.e., I_{max}. Limiting the current references is the simplest way to prevent over-currents. A q-axis-priority current saturation logic is as follows

$$\begin{cases} |i_{q,ref}| = \min(I_{max}, |i^*_{q,ref}|) \\ |i_{d,ref}| = \min(\sqrt{I^2_{max} - i^2_{q,ref}}, |i^*_{d,ref}|). \end{cases} \qquad (3)$$

A d-axis-priority current saturation can be achieved by swapping d− and q−components in (3). As the current reference saturation might lead to windup in the outer loops resulting in phase drift and transient instability of the GFMI [19], power references should be reduced during voltage sags. Moreover, adjusting the power references during faults can restrain the power angle evolution [27]; hence expanding the critical clearing time of a fault [25]. Therefore, a power reference adjustment loop, adopted from [1] and [28], is added to the GFMI's control to restrain the power references during faults. During a symmetrical fault, the apparent power set-point of the GFMI is modified to [1]

$$S_{new} = V_{pu}S_n, \qquad (4)$$

where $V_{pu} = \frac{\sqrt{6}}{2V_0}\sqrt{v^2_{g,d} + v^2_{g,q}}$, and S_n denotes the GFMI's nominal power. Reactive and active power references are then, respectively, updated according to [1]

$$Q^* = \begin{cases} Q_{set}, & \text{if } V_{pu} > 0.9 \\ 2S_{new}(1 - V_{pu}), & \text{if } 0.5 < V_{pu} < 0.9 \\ S_{new}, & \text{if } V_{pu} < 0.5 \end{cases} \qquad (5)$$

and

$$P^* = \begin{cases} P_{set}, & \text{if } V_{pu} > 0.9 \\ \sqrt{S^2_{new} - Q^{*2}}, & \text{if } V_{pu} < 0.9 \end{cases} \qquad (6)$$

where P_{set} and Q_{set} are the active and reactive power set-points of the GFMI in the normal operation, respectively.

C. Post-fault Oscillation Phenomenon

Post-fault oscillations have been reported in [1], [15], [16]. In [15], the VSI switches from a voltage-controlled mode to a current-controlled mode when a voltage sag is detected, which causes oscillations in the active and reactive power responses. Hence, remaining in a voltage-controlled mode during faults helps avoid the additional oscillation caused by control mode transitions. Additionally, as described in [16], non-ideally-tuned controllers of the VSI in Type-4 wind turbines and their supporting devices, e.g., synchronous condensers, can lead to overshoots
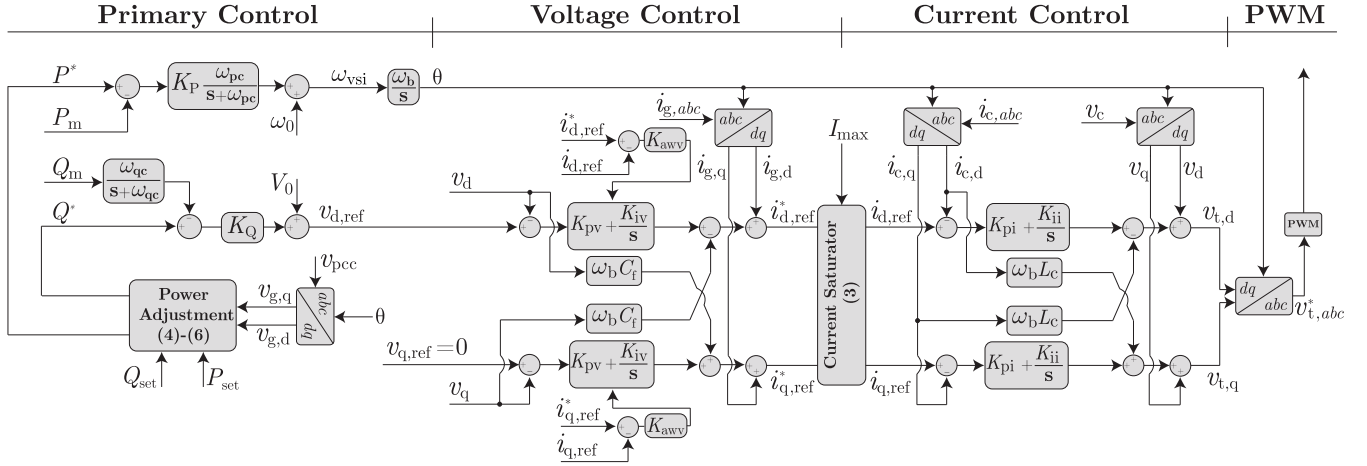
Fig. 2. Control diagram of the droop-controlled GFMI with the Current Saturator and the Power Adjustment.

and oscillations in the voltage. If the gains of the voltage controller in the VSI are too low, the slow reaction of the VSI might fail to suppress the post-fault voltage overshoot. In contrast, voltage oscillation can be a consequence of an extremely high-gain voltage controller. Synchronous condensers and static VAR compensators can enhance the post-fault responses of the VSI [16]. However, they require additional cost and tuning. Tuning the VSI control can improve the poor post-fault transients in a specific operating condition. However, the network configuration and the VSI's operation are not static. Hence, a more robust solution is required [16]. In [1], post-fault oscillations are present in the current responses, reflecting oscillatory power transients of the VSI. Hence, VR is added to the VSI control in the recovery phase to dampen those oscillations [1]. Nevertheless, the effects caused by the VR on the fault recovery in different grid strength conditions are not detailed in [1]. In addition, as the power and voltage dynamics are dependent on the network configuration [16], [25], using a fixed-value VR in all grid strength conditions is not an optimal solution.

When the grid is weak, v_{pcc} and v_c are more sensitive to changes in the current and the power flowing between the VSI and the grid [1], [16]. Therefore, the post-fault oscillations become more severe in weak grids. In addition, according to [18], when the grid impedance increases, the system damping reduces, leading to oscillatory behaviors of voltage and power.

Post-fault responses of a GFMI under different grid strength conditions are shown in Fig. 3. The grid strength is measured by the SCR, which is calculated as [3]

$$\text{SCR} = \frac{V_0^2}{Z_s S_{\text{rate}}} = \frac{1}{Z_{s,\text{pu}}}, \quad (7)$$

where Z_s and $Z_{s,\text{pu}}$ are the network impedance and its per-unit value, and S_{rate} is the rated power of the inverter [3]. The GFMI's parameters can be found in Table I. A three-phase bolted fault occurs at 0.1 s and is cleared at 0.3 s. Following the fault clearance are oscillatory transients in the active and reactive power, the voltages, and the currents of the GFMI. The magnitude and the duration of the oscillations reduce as the short circuit ratio (SCR) of the grid increases. Although the GFMI remains stable eventually, the poor transients can trigger protection devices resulting in unnecessary disconnections of the GFMI from the grid.
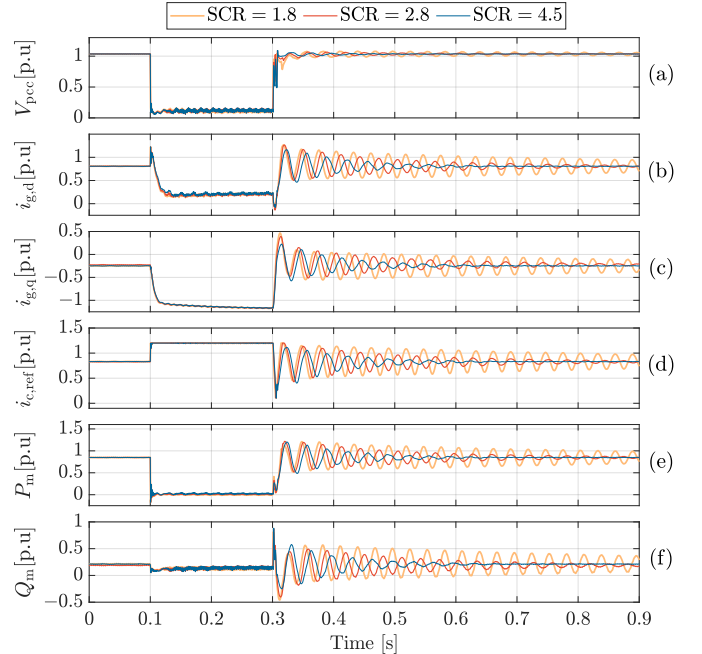
Fig. 3. Simulated post-fault responses of the GFMI, whose parameters are listed in Table I, with different SCRs: (a) the magnitude of the PCC voltage, (b) the d-component of the grid current, (c) the q-component of the grid current, (d) the magnitude of the inverter-side current reference, (e) the active power at the PCC, and (f) the reactive power at the PCC.

III. POST-FAULT DAMPING BY VIRTUAL RESISTANCE

In this section, a fixed-value VR (FVR) model is introduced first, and several negative impacts of the FVR are revealed. An AVR model is then proposed to mitigate those impacts caused by the FVR, yet still sufficiently dampen the post-fault oscillations.

A. Fixed-value Virtual Resistor

In [1], a dynamic VR model, which is implemented in an α-β frame with SPC, is introduced. The FVR presented in this section is adopted from [1] and modified to be compatible with an SRF and droop control. The FVR operates in a trigger-reset manner. When a voltage recovery is detected, e.g., the voltage rises and crosses 0.85 pu, the VR is immediately added to the control. The VR is held at a constant value for a short interval of time before ramping down to zero at a predefined rate. This temporary VR does not affect the normal operation of the GFMI, yet providing

Fig. 4. Virtual resistor implementation in a Synchronous Reference Frame.

Fig. 5. Simplified voltage control diagram.

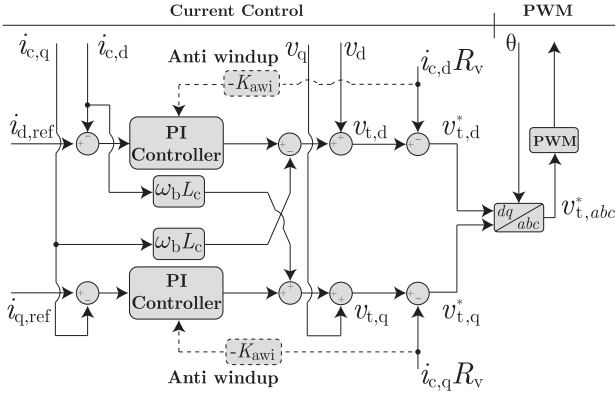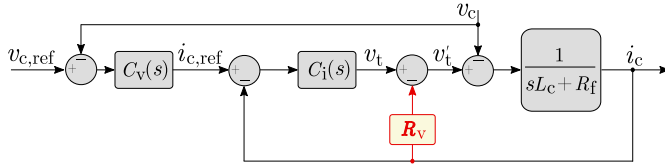a damping effect in the fault-recovery phase. Usually, the VR is implemented by subtracting virtual voltage drops over the VR from $v_{d,ref}$ and $v_{q,ref}$ [25], [27], before feeding those references to the voltage control loop. Therefore, the voltage set-points in the dq-frame become

$$\begin{cases} v_{d,ref}^* = v_{d,ref} - i_{c,d}R_v, \\ v_{q,ref}^* = v_{q,ref} - i_{c,q}R_v, \end{cases} \quad (8)$$

where $v_{d,ref}^*$ and $v_{q,ref}^*$ denote the actual references of the voltage control loop, and R_v is the virtual resistance.

The GFMI recovers at a relatively fast rate from a fault. However, the limited bandwidth of the voltage control loop causes delays in propagating the damping effect of the VR to the actual currents and voltages. Hence, the VR cannot suppress the very first overshoots right after the fault clearance. To accelerate the application of the VR, the VR implementation should be moved to the terminal voltages as

$$\begin{cases} v_{t,d}^* = v_{t,d} - i_{c,d}R_v, \\ v_{t,q}^* = v_{t,q} - i_{c,q}R_v, \end{cases} \quad (9)$$

where $v_{t,d}^*$ and $v_{t,q}^*$ are the dq-components of the references for the pulse width modulation (PWM). By this approach, the VR becomes active immediately after the fault clearance; hence avoiding the slow dynamic caused by the cascade control loops.

The VR in this work resembles an additional amount of internal series resistance of the converter-side inductor, i.e., L_c. This resemblance can be verified by looking at the output impedance of the GFMI with and without the VR activation. Based on the simplified control diagram shown in Fig. 5, the expressions of the GFMI output impedance with and without the VR are

$$Z_{VR}(s) = \frac{v_c}{i_c} = -\frac{(L_c s + R_f + R_v) + C_i}{1 + C_v C_i} \quad (10)$$

and

TABLE I. Simulation and Experimental parameters.

Parameter	Simulation	Experiment
Nominal Power (kVA)	35	1.3
Nominal Voltage (V)	400	90
ω_b (rad/s)	$2\pi 50$	$2\pi 50$
L_c, C_f, L_g (pu)	0.09, 0.049, 0.076	0.34, 0.12, 0.2
Z_{g1}, Z_{g2} (pu)	$0.1j$, (0.12 - 0.45)∠86°	0, (0.2 - 0.47)∠85°
f_{switch} (kHz)	10	10
$T_{sampling}$ (μs)	50	50
P_{set}, Q_{set} (pu)	0.85, 0	0.91, 0
K_P, K_Q (pu)	0.02, 0	0.039, 0
ω_{pc}, ω_{qc} (rad/s)	32	32
ω_0 (pu)	1	1
V_0 (pu)	1.06	1.06
K_{pv}, K_{iv}, K_{awv}	0.08, 14, 110	0.12, 6.76, 563
K_{pi}, K_{ii}, K_{awi}	2.6, 26, 2	4.7, 140, 6
ω_h (rad/s)	300	300
ω_f, ω_s (rad/s)	1256, 125.6	1256, 125.6
T_2, T_3 (ms)	200	500
K	185×10^{-6}	0.0045

$$Z_{noVR}(s) = \frac{v_c}{i_c} = -\frac{(L_c s + R_f) + C_i}{1 + C_v C_i}, \quad (11)$$

respectively, where R_f is the physical internal resistance of L_c, and C_v and C_i are the voltage and the current controllers, respectively. The VR value, i.e., R_v, appears in the output impedance similarly to a physical series resistor as shown in (10). Thus, the implementation of the VR on the terminal voltage provides the same effect as adding a physical resistor. The added resistor is placed in series with L_c, before the filter capacitor, C_f, and does not make any changes in the voltage reference. Thus, it is not expected to change the output voltage level like the VR designed for the current limiting purpose [25]. Instead, the main function of the VR in this work is improving the system damping to suppress the post-fault oscillations. The effectiveness of the VR in enhancing the system damping is presented and validated in Section III-D and Section IV.

Additionally, subtracting the virtual voltage drops from $v_{t,d}$ and $v_{t,q}$ is analogous to limiting the PI controllers' outputs in the current control loop. This leads to windup and can further degrade the transients. As a result, it is necessary to equip these PI controllers with an anti-windup algorithm. Back-calculation anti-windup is utilized in this study to mitigate the negative impacts of the VR [29]. The implementation of the VR in an SRF is summarized in Fig. 4. The AVR, which is proposed in Section III-C, is also integrated into the GFMI control in the same manner as shown in Fig. 4. The only difference between the FVR and the AVR is how R_v is determined. The shape of the FVR with respect to time is shown in Fig. 8. Regardless of variations in the network, the constant value of the FVR remains unchanged in all cases. This fact might lead to an unnecessary damping effect; hence resulting in a slow recovery or even instability of the GFMI when the grid is stiff. More details on the problems caused by the FVR are discussed in Section III-B.

B. Problems Caused by the Fixed-value Virtual Resistor

Introducing too much virtual resistance to the system has been reported negatively impacting the system small-signal stability [18], [19]. Moreover, the large-signal stability of the GFMI is also affected by the presence of the VR, especially when the current saturator is utilized. Furthermore, the VR is applied in

the fault recovery process, in which the GFMI is in a transient phase and extremely vulnerable. An inappropriate value of the VR can degrade the recovery or even cause instability. In this section, the large-signal instability caused by the FVR in various grid strength conditions is investigated.

With the presence of the VR, the GFMI has to generate more active power to compensate for the virtual power loss caused by the VR. As a result, higher reference currents are necessary to reach the power set-point. Besides, in the recovery phase, a large amount of reactive current is needed for restoring the voltage. Therefore, the current reference is likely to saturate with the presence of the VR in this phase. Current reference saturation can lead to phase drift and instability [19]. In addition, the dynamic equation of the phase angle between v_{pcc} and v_{g} is [11]

$$\ddot{\delta} = -\omega_{\text{pc}}{}^2 \frac{K_{\text{P}}}{s + \omega_{\text{pc}}}(P^* - P_{\text{m}}) + \omega_{\text{pc}}K_{\text{P}}(P^* - P_{\text{m}}) \quad (12)$$

$$\Rightarrow \ddot{\delta} = (1 - \frac{\omega_{\text{pc}}}{s + \omega_{\text{pc}}})\omega_{\text{pc}}K_{\text{P}}(P^* - P_{\text{m}}). \quad (13)$$

During a fault recovery, a large amount of reactive current is required to restore the voltage. If a large VR is used, more active current is required to recover the PCC power to its set-point, as the virtual power loss caused by the VR is higher. As both active and reactive currents are in high demand, the output current is more likely to saturate again after the fault clearance. Once the current saturates, P_{m} cannot recover as fast as in the case without the saturation. Therefore, with a large VR, P_{m} recovers slowly, resulting in a slow reduction in $(P^* - P_{\text{m}})$; hence preventing $\ddot{\delta}$ from converging to zero. Consequently, the fault recovery process becomes longer. Therefore, excessive virtual resistance applied in the fault-recovery process potentially degrades the recovery or even results in system instability.

In Fig. 3, the weaker the network is, the more severe the post fault oscillations are. Hence, to cope with the worst-case scenario, the VR is tuned such that it can dampen the oscillations in the lowest possible SCR condition without destabilizing the GFMI. However, the grid topology is not static. For instance, line switchings may lead to grid strength variations. Therefore, the impacts of the VR should be studied in higher-SCR networks as well. To simplify the analysis, Z_{g1}, Z_{g2}, and L_{g} are combined to represent the grid impedance, denoted as Z_{g}, i.e., $Z_{\text{g}} = Z_{\text{g1}} + Z_{\text{g2}} + \omega_{\text{b}}L_{\text{g}}$. After the fault clearance, to regulate $|v_{\text{c}}|$ at the voltage reference $v_{\text{d,ref}}$, the required grid current is given as

$$i_{\text{g}} = \frac{v_{\text{d,ref}}\angle\delta_1 - v_{\text{g}}}{Z_{\text{g}}}, \quad (14)$$

where δ_1 is the instantaneous power angle after the fault. v_{g} is assumed to be equal to 1 pu. When Z_{g} decreases, a higher grid current is needed to boost v_{c} to its set-point. The strong coupling between v_{g} and v_{c} in higher-SCR networks might cause current saturation. As aforementioned, the current saturation can make the system unstable. However, in the very first instants after the fault clearance, a stiff grid allows v_{c} to rise quickly toward 1 pu; hence the voltage error diminishes rapidly. As a result, the current references rise more slowly compared to a weak grid. If the VR reduces or is deactivated before the current saturates, instability can be avoided.

To visualize how the FVR impacts the fault recovery in various grid-strength conditions, a set of simulation tests has been run to
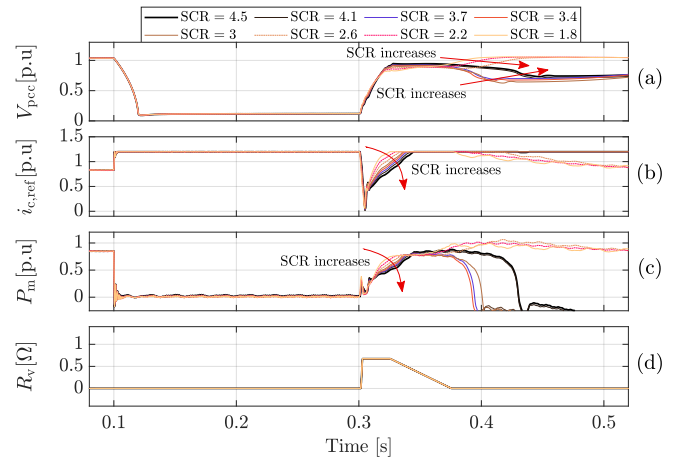

Fig. 6. Impact of an FVR on the responses of a GFMI to a three-phase bolted fault with SCR varying from 1.8 to 4.5: (a) the magnitude of the PCC voltage, (b) the inverter output current set-point, (c) the active power transfer measured at the PCC, and (d) the value of virtual resistance.

show how a GFMI behaves when the SCR gradually increases from 1.8 to 4.5 in the presence of an FVR. The control and system parameters of the simulations are summarized in Table I. A three-phase bolted fault is applied at 0.1 s and cleared at 0.3 s. The FVR is held at 0.675 Ω for 25 ms before ramping down to zero at a rate of 20 Ω/s. Although the VR is implemented on the terminal voltage right before the PWM, it still takes a few milliseconds since the fault clearance instant for the VR to be active. Before the activation of the VR, the system damping is still low. Hence, the first swing of the post-fault oscillation still occurs. It causes the sudden drop in $i_{\text{c,ref}}$ right after the fault clearance, as depicted in Fig. 6. Subsequently, the activation of the VR suppresses the rest of the oscillation and slows down the variation of $i_{\text{c,ref}}$ and P_{m}. As shown in Fig. 6, when the SCR increases, the saturation in the current reference, i.e., $i_{\text{c,ref}}$, becomes more severe and lasts longer. As a result, the recovery is slower and degraded. Starting from an SCR of 3, the active power, i.e., P_{m}, collapses after the fault and the GFMI becomes unstable.

In conclusion, the FVR is not a robust solution for post-fault oscillation damping. A value of VR that is well functional in a weak grid can cause severe current saturation, degrade the recovery or even result in instability when the grid strength increases. To obviate this issue, in the next section, an adaptive VR is proposed.

C. Adaptive Virtual Resistor for Post-fault Oscillation Damping

As the FVR performs differently when the grid strength varies, knowledge of grid strength is beneficial for setting an appropriate value for the VR. Nevertheless, measuring grid impedance is challenging, and the grid impedance is not static. Hence, an adaptive solution is necessary. Due to the problems caused by the FVR as discussed in Section II-B, in this section, an AVR is presented to suppress the post-fault oscillatory transients in various grid conditions without destabilizing the GFMI.

As mentioned in [1], [16] and shown in Fig 3, the severity of the post-fault power oscillation varies as the network strength changes. If the VR is set according to the intensity of the power oscillations, it can be self-adjusted to avoid over-dampening the
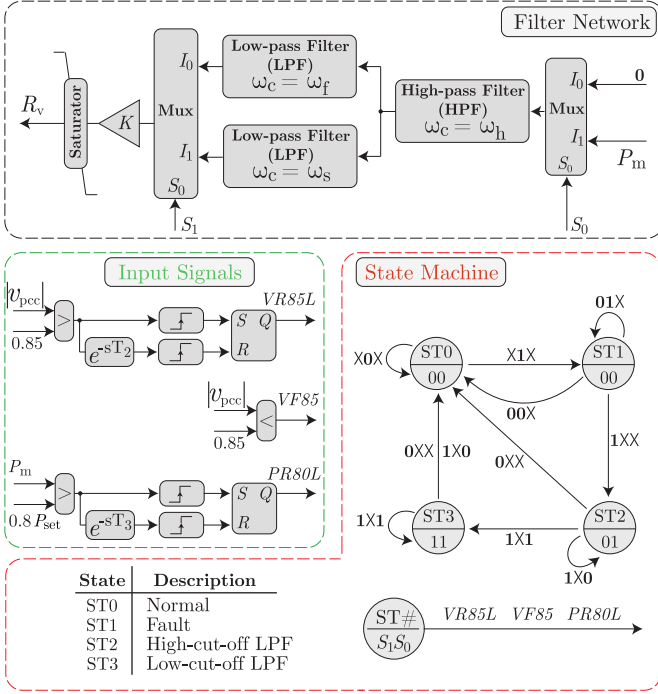
Fig. 7. Adaptive virtual resistor calculation: R_v is determined by a Filter Network, which is controlled by a State Machine (SM) via $S_1 S_0$. Input Signals to the SM depend on $|v_{pcc}|$ and P_m.

power response unnecessarily. When the oscillation is significant, more virtual resistance is integrated into the control to dampen the oscillatory transient. Whereas, if the oscillatory transient is not too severe, less virtual resistance is utilized. Moreover, when the power settles after the fault, the oscillation magnitude gradually diminishes to zero, leading to a smooth removal of the AVR. The AVR calculation is summarized in Fig. 7. It consists of two main parts: a *filter network* and a *state machine* that controls the filter network.

1) Filter Network: The severity of the post-fault oscillations is determined by the rate of change of the active power, which is estimated by a combination of filters, as shown in Fig. 7. The AVR is active when the signal S_0 is set to 1. While the AVR is active, P_m is first passed through a high-pass filter (HPF), whose transfer function is

$$H_{hpf} = \frac{s}{s + \omega_h}, \tag{15}$$

with a cut-off frequency of ω_h rad/s. A first-order HPF is utilized for taking advantage of its wide roll-off to capture most of the power dynamics with a focus on fast variations. Its output is then smoothened by either of the low-pass filters (LPFs) depicted in Fig. 7, depending on the signal S_1. A filter type with narrow roll-off is beneficial for rejecting undesired harmonics in this case. Hence, second-order low-pass Butterworth filters can be used for the LPFs, whose transfer function is

$$H_{lpf} = \frac{\omega_c^2}{s^2 + \sqrt{2}\omega_c s + \omega_c^2}, \tag{16}$$

where ω_c is the cut-off frequency. As depicted in Fig. 7, the resistance of the AVR can be adjusted by the constant K, whose tuning is discussed in Section III-C3. To prevent the AVR from degrading the fault recovery unnecessarily, the outputs of the LPFs are bounded by a saturator. The limits of the saturator are

detailed in Section III-C3. The output of the saturator is R_v. The operation of the filter network is governed by S_1 and S_0, which are generated by the state machine presented in the following section.

2) State Machine: The state machine, shown in Fig. 7, outputs S_1 and S_0 to control the operation of the filter network. There are four states in the state machine, including Normal (ST0), Fault (ST1), High-cut-off LPF (ST2), and Low-cut-off LPF (ST3).

- **ST0:** In the normal operation of the GFMI, because $|v_{pcc}|$ is greater than 0.85 pu, the signal *VF85* is 0, and the GFMI remains in ST0. $S_1 S_0$ equals 00 in this state.
- **ST1:** When a fault occurs, and $|v_{pcc}|$ goes below 0.85 pu, *VF85* becomes 1. In this case, the GFMI transits to the Fault state (ST1) and remains there until $|v_{pcc}|$ recovers to 0.85 pu. $S_1 S_0$ equals 00 in this state.
- **ST2:** When $|v_{pcc}|$ rises and crosses 0.85 pu, *VR85L* is set to 1 and held for T_2 seconds, hence activating the AVR and transiting the control to ST2. S_0 rises to 1 due to this transition. T_2 defines the maximum duration of the AVR. In ST2, a wider-bandwidth LPF, with a cut-off frequency of ω_f, is first used to dampen the fast dynamics in the early stage of the power recovery. $S_1 S_0$ equals 01 in this state.
- **ST3:** When the power recovers and exceeds 80% of the power set-point, *PR80L* is set to 1 and held for T_3 seconds, transiting the control to ST3 and S_1 to 1. In ST3, the AVR is determined by a narrower-bandwidth LPF, with a cut-off frequency of ω_s to avoid amplifying harmonics and possible sub-synchronous oscillations in the system [30]. T_3 defines the duration of ST3. $S_1 S_0$ equals 11 in this state.

  When either T_2 or T_3 elapses, the control returns to ST0.

3) Parameters Tuning: This section presents a guideline for tuning the parameters of the AVR, including ω_f, ω_s, ω_h, and K. At the beginning of a fault recovery process, i.e., in ST2, the power rises relatively fast, potentially leading to the highest overshoot. The wider-bandwidth LPF must be able to capture the fast dynamics of the active power in this state. Due to the zero-crossing breaking mechanism of circuit breakers, the power in all three phases usually recovers in 7-10 ms after the first phase is tripped. To capture the fast power dynamics right after the fault clearance, ω_f can be set between 628 rad/s (100 Hz) and 1256 rad/s (200 Hz). On the other hand, in ST3, the power almost settles down, and its dynamics becomes slower. The high cut-off frequency of the LPF in ST3 is unnecessary. Moreover, since most of the active time of the AVR is in ST3, the high cut-off frequency might result in amplifications of the undesired sub-synchronous harmonics as aforementioned [30]. To avoid these undesired amplifications, ω_s should be set between 31 rad/s (5 Hz) and 125.6 rad/s (20 Hz). Finally, to acquire the whole dynamic profile of the power recovery, ω_h should be a few times lower than ω_f.

Since the post-fault oscillations are most severe in the weakest grid condition, K should be tuned to dampen the transients in the lowest possible SCR condition. Besides, as the AVR is the largest in this condition, the current reference is most likely to saturate. Therefore, designing the AVR in the weakest grid condition should be well considered. K should be chosen such that the resulting R_v does not make the maximum power measured at the PCC drop below 95% of the power set-point. The maximum
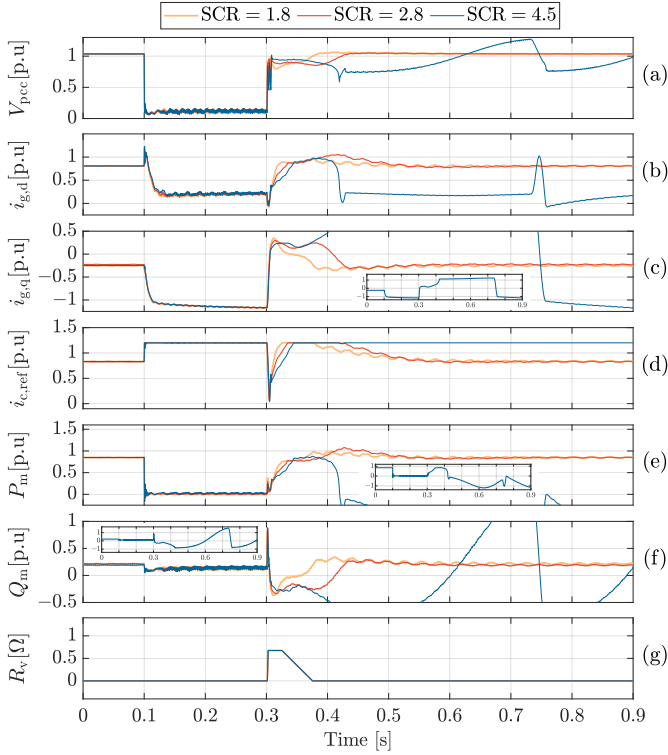
Fig. 8. Simulated post-fault responses of the GFMI with the fixed-value VR for oscillation damping in different grid strength conditions: (a) the magnitude of the PCC voltage, (b) the d-component of the grid current, (c) the q-component of the grid current, (d) the magnitude of the inverter-side current reference, (e) the active power at the PCC, (f) the reactive power at the PCC, and (g) the virtual resistance.

power at the PCC can be calculated as

$$P_{\max} = \frac{|v_{\mathrm{pcc}}|}{Z_{\mathrm{f}}} [|v_{\mathrm{t}}| - |v_{\mathrm{pcc}}| \cos(\phi)], \tag{17}$$

where

$$Z_{\mathrm{f}} = \sqrt{(\omega_{\mathrm{b}} L_{\mathrm{c}} + \omega_{\mathrm{b}} L_{\mathrm{g}})^2 + R_{\mathrm{v}}^2}, \\ \phi = \arctan(\frac{(\omega_{\mathrm{b}} L_{\mathrm{c}} + \omega_{\mathrm{b}} L_{\mathrm{g}})}{R_{\mathrm{v}}}). \tag{18}$$

$|v_{\mathrm{pcc}}|$ and $|v_{\mathrm{t}}|$ can be approximated by the constant nominal voltage, i.e., V_0. If the cut-off frequencies of the filters are set as aforementioned, due to the attenuating effect of the filters, the output of the LPFs usually falls to between 20% and 50% of the steady-state power set-point. K can be set accordingly to obtain the desired virtual resistance value such that the condition on the maximum power at the PCC is satisfied. The limits of the saturator in the filter network can be set to ensure that the AVR does not make the maximum power at the PCC drop below 95% of the power set-point.

To cope with asymmetrical faults, negative sequence controls should be added to the system [31]. The AVR can then be applied to both positive and negative sequence controls. However, due to space limitation, the application of the AVR in unbalanced conditions is not presented in this paper.

D. Damping Provided by a Virtual Resistor to Suppress Post-fault Oscillation.

To justify if the R_{v} value is sufficient to dampen the oscillations, firstly, the oscillation modes in the network area should
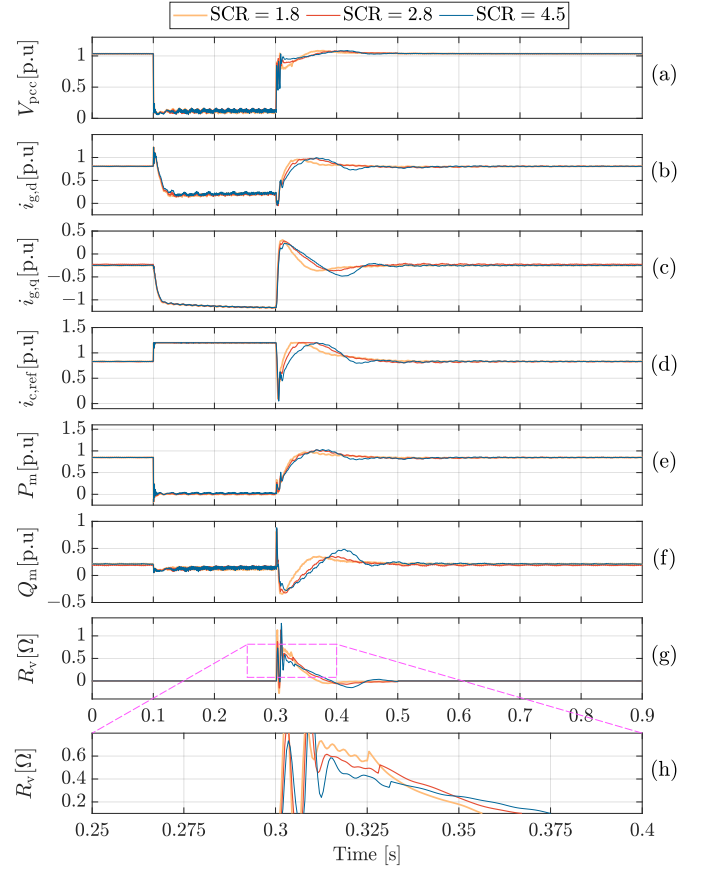

Fig. 9. Simulated post-fault responses of the GFMI with the adaptive VR for oscillation damping in different grid strength conditions: (a) the magnitude of the PCC voltage, (b) the d-component of the grid current, (c) the q-component of the grid current, (d) the magnitude of the inverter-side current reference, (e) the active power at the PCC, (f) the reactive power at the PCC, (g) the virtual resistance, and (h) the magnified view of the virtual resistance.

be identified. This can be done by applying Prony analysis or FFT on a recorded response of the system after a contingency as mentioned in [32]. The post-fault oscillations propagate from the voltage loop and the grid currents, i.e., i_{gd} and i_{gq}, to the inner current loop. As a result, $i_{\mathrm{d,ref}}$ and $i_{\mathrm{q,ref}}$ are distorted with the oscillations. If the current loop provides enough damping on the oscillations, the oscillations are attenuated before propagating to the PWM block. To investigate the damping provided by the current loop, its closed-loop transfer function should be obtained. The PI controller in the current control loop is chosen as $\frac{K_{\mathrm{i}}(L_{\mathrm{c}}s + R_{\mathrm{f}})}{s}$, where K_{i} is a constant gain. Therefore, the closed-loop transfer function of the current loop becomes

$$G_{\mathrm{i}}(s) = \frac{i_{\mathrm{c}}}{i_{\mathrm{c,ref}}} = \frac{K_{\mathrm{i}}(L_{\mathrm{c}}s + R_{\mathrm{f}})}{L_{\mathrm{c}}s^2 + (K_{\mathrm{i}}L_{\mathrm{c}} + R_{\mathrm{f}} + R_{\mathrm{v}})s + K_{\mathrm{i}}R_{\mathrm{f}}}, \tag{19}$$

where i_{c} and $i_{\mathrm{c,ref}}$ are the output current of the inverter and its reference, respectively. Hence, the damping ratio of the current loop is

$$\zeta = \frac{K_{\mathrm{i}}L_{\mathrm{c}} + R_{\mathrm{f}} + R_{\mathrm{v}}}{2\sqrt{K_{\mathrm{i}}R_{\mathrm{f}}L_{\mathrm{c}}}}. \tag{20}$$

It can be seen that varying the value of R_{v} can change the damping provided by the current control loop. An adequate value of R_{v} should apply sufficient damping on the identified oscillation modes, i.e., below -3 dB.

Moreover, during the recovery process, the AVR dynamically changes the value of R_v based on the oscillation magnitude. Therefore, R_v is not constant during its active time. The AVR is similar to a feedback damping mechanism. In the early stage of the recovery, a larger R_v is required to suppress the first and also the highest overshoot in the responses. Subsequently, smaller R_v is preferable to dampen lower-magnitude oscillations while not degrading the recovery. An example of the above discussions can be found in Section IV-A.

IV. PERFORMANCE EVALUATION

A. Simulation Results

The tests used for generating the results in Fig. 3 are replicated with the presence of the FVR and the AVR. These tests aim at showing and comparing the impacts of the FVR and the AVR on post-fault responses of a GFMI in different grid strength conditions. The system and control parameters are listed in Table I. The steady-state power set-point is 0.85 pu. At 0.1 s, a three-phase bolted fault occurs and lasts for 200 ms. Either FVR or AVR is activated to dampen the post-fault oscillations in the recovery process. The FVR is kept at 0.675 Ω for 25 ms before ramping down at a rate of 20 Ω/s. The details of the AVR are listed in Table I.

The results of the FVR are presented in Fig. 8. When the grid SCR equals 1.8 and 2.8, the system can recover after the fault clearance. Compared to the responses without any types of VR, as shown in Fig. 3, lower overshoots and better-damped responses of V_{pcc}, i_{dq}, P_m, and Q_m can be seen with the FVR being active. However, in a stiffer grid with SCR equal to 4.5, the power P_m collapses shortly after the fault clearance due to a severe saturation in the current reference, i.e., $i_{c,ref}$, as discussed in Section III-B, although the GFMI can recover if no FVR is in service as shown in Fig. 3. In Fig. 8, small subplots, showing the complete responses of $i_{g,q}$, P_m, and Q_m when the SCR equals 4.5, are included. Apart from that, as shown in Fig. 8, for SCR levels equal to 1.8 and 2.8, even though the FVR improves the responses, small oscillations still persist in all the responses after the system settles.

In Fig. 9, the results of the AVR are displayed. In all grid strength conditions, the responses of V_{pcc}, i_{dq}, P_m, and Q_m

Fig. 11. Experimental setup.

can smoothly recover to their pre-fault values without significant overshoots. All the post-fault responses are almost oscillation-free. R_v is adjusted according to the active power recovery rates; hence preventing degrading the recovery process in higher SCR conditions. As discussed in Section III-C, R_v reduces as the grid SCR increases. Thanks to this self-adjustment of the AVR, $i_{c,ref}$ does not saturate when SCR equals 4.5 as opposed to the FVR. Hence, instability is avoided. Even though $i_{c,ref}$ saturates when SCR equals 1.8 or 2.8, the saturation levels are not as severe as those caused by the FVR. Eventually, $i_{c,ref}$ reduces to the normal operating point.

From the time-domain responses of the GFMI, when R_v is set to zero, depicted in Fig. 3, the dominant oscillation mode's frequency is estimated between 190 rad/s and 220 rad/s. This range is highlighted in Fig. 10. In this frequency range, the magnitude of G_i, presented in (19), with R_v being equal to 0 Ω is between -0.03 dB and -0.05 dB. That is why the under-damped behaviors are observed in the system responses. As shown in Fig. 9, when the AVR is active, the highest value of R_v at the
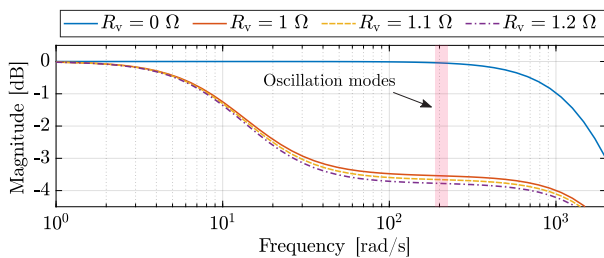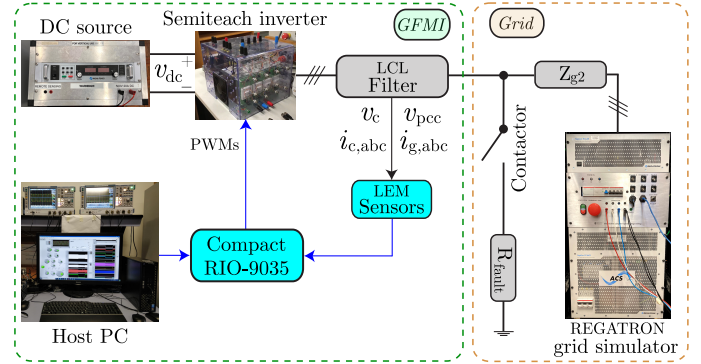

Fig. 10. Closed-loop response of the current loop, i.e., $G_i(s)$, with different R_v values.

TABLE II. Quantitative comparison among the active power results in the simulation tests.

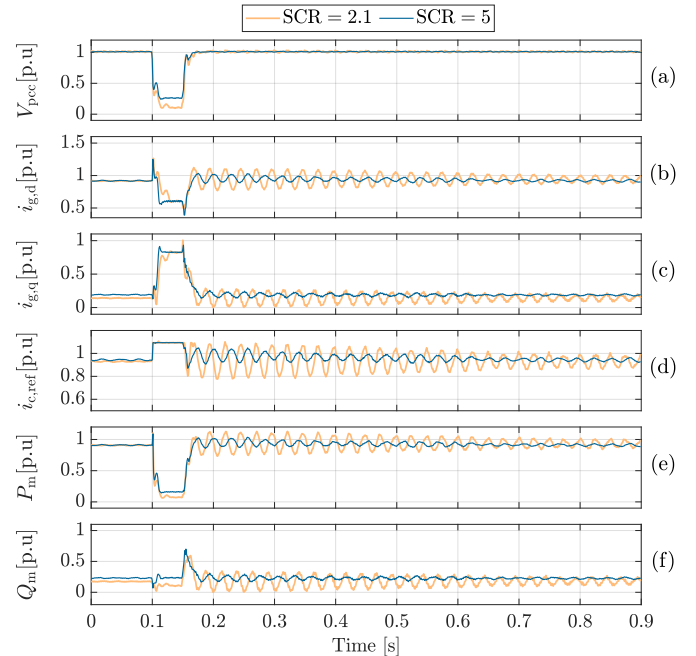| Type of VR	Overshoot (%)	Settling time (s)
None (SCR: 1.8, 2.8, 4.5)	42, 43, 41	2.06, 0.62, 0.3
FVR (SCR: 1.8, 2.8, 4.5)	16, 26, unstable	0.46, 0.42, unstable
AVR (SCR: 1.8, 2.8, 4.5)	15, 20, 20	0.16, 0.3, 0.25

Fig. 12. Measured post-fault responses of the experimental GFMI without VR for oscillation damping in different grid strength conditions: (a) the magnitude of the PCC voltage, (b) the d-component of the grid current, (c) the q-component of the grid current, (d) the magnitude of the inverter-side current reference, (e) the active power at the PCC, and (f) the reactive power at the PCC.

Fig. 13. Measured post-fault responses of the experimental GFMI with the FVR for oscillation damping in different grid strength conditions: (a) the magnitude of the PCC voltage, (b) the d-component of the grid current, (c) the q-component of the grid current, (d) the magnitude of the inverter-side current reference, (e) the active power at the PCC, (f) the reactive power at the PCC, and (g) the virtual resistance.
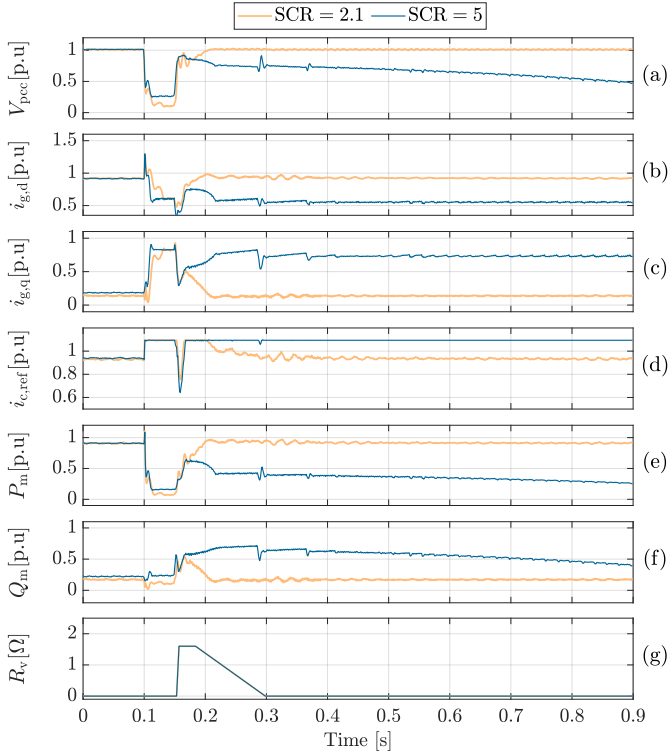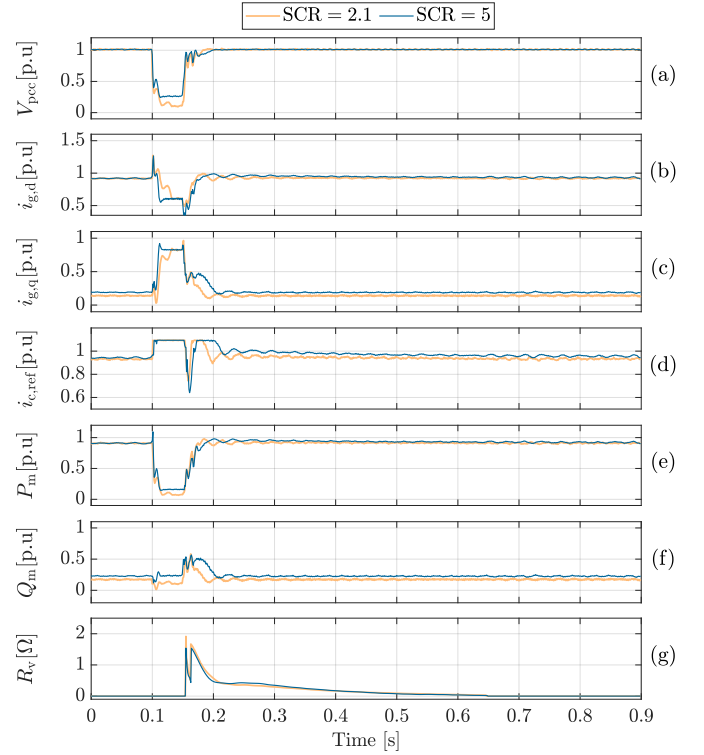

Fig. 14. Measured post-fault responses of the experimental GFMI with the AVR for oscillation damping in different grid strength conditions: (a) the magnitude of the PCC voltage, (b) the d-component of the grid current, (c) the q-component of the grid current, (d) the magnitude of the inverter-side current reference, (e) the active power at the PCC, (f) the reactive power at the PCC, and (g) the virtual resistance.

beginning of the recovery is between 1 Ω and 1.2 Ω. With an R_{v} value in this range, the magnitude of G_{i} varies between -3.6 dB and -3.8 dB. As a result, the time-domain response is critically damped when the AVR is activated.

A quantitative comparison among the power responses in the cases with the FVR, the AVR, and without neither is summarized in Table II. In general, the AVR results in significant reductions in both the overshoot and the settling time of the active power responses. Overall, the AVR can effectively dampen the post-fault oscillatory transients and is robust against variations in the grid SCR level.

B. Experimental Results

The performance of the proposed AVR model is validated in a laboratory experimental setup, as depicted in Fig. 11. The grid-forming control and the AVR are implemented in a National Instrument (NI) CompactRIO-9035 controller to drive a Semikron SemiTeach inverter. The inverter is connected to a Regatron TC.ACS grid simulator via an LCL filter and a three-phase inductor, i.e., Z_{g2}, which emulates the line impedance. The currents and voltages are measured by LTSR 15-NP and DVC 1000-P LEM sensors, respectively, and sampled by a NI 9020 ADC module. A fault is created by connecting the PCC to the ground via a low-resistive path. A three-phase contactor is employed to manipulate the fault occurrence and the fault duration. All the parameters of the setup can be found in Table I.

In the steady-state, the active power set-point is set to 0.91 pu. At t = 0.1 s, a symmetrical fault is applied by closing the contactor shown in Fig. 11. The fault resistor, i.e., R_{fault}, is 1 Ω

for each phase. After 50 ms, the contactor opens, emulating a fault clearance event.

The GFMI is tested in two different grid strength conditions: SCR = 2.1 and SCR = 5. Since the fault resistor is fixed in the two cases, while the line impedance is changed in each condition to achieve the aforementioned SCRs, the residual voltage and the active power during the fault are different in each case, as shown in Fig. 12, Fig. 13, and Fig. 14.

In Fig. 12, without the AVR, although the GFMI can recover from the fault in both the grid strength conditions, oscillations persist in all the responses of the GFMI when the SCR equals 2.1. These oscillations last for 1 s after the fault clearance instant. The oscillations' magnitude and duration reduce as the SCR increases to 5. These behaviors align with the analysis in Section II-C and the simulation results.

To mitigate the post-fault oscillatory transients, an FVR is activated after the fault clearance. The FVR is kept at 1.6 Ω for 30 ms before ramping down at a rate of 13 Ω/s. The result of this test is presented in Fig. 13. In the low-SCR case, the FVR successfully dampens the post-fault oscillations. However, when the SCR rises to 5, due to the problems mentioned in Section III-B, the current reference, i.e., $i_{\mathrm{c,ref}}$, saturates and remains at the maximum current value, as shown in Fig. 13(d). This prevents the GFMI from lifting its active power to the pre-fault level and re-synchronizing with the grid, as depicted in Fig. 13(e). As a result, the active power and the voltage collapse after 50 ms, and the GFMI becomes unstable.

With the activation of the AVR, in the low-SCR case, the oscillations in all the waveforms are well damped, as presented in Fig. 14. P_{m} and i_{dq} settle within 50 ms after the fault clearance.

Moreover, the highest oscillation magnitude in P_m is only one-fourth of the counterpart in the case without the VR. When the SCR equals 5, the oscillations' magnitude is less significant compared to those in the low-SCR case. These oscillations are quickly dampened even in the case without the VR. Hence, R_v is lower in the early stage of the fault recovery process compared to that in the low-SCR case. With the AVR being active, $i_{c,ref}$ also saturates after the fault clearance due to high R_v values at the beginning of the recovery. However, once P_m starts settling down and the oscillations are suppressed, R_v reduces and $i_{c,ref}$ returns to its steady-state value as shown in Fig. 14(d). Actually, if R_v in the case with the FVR ramps down to zero at a faster rate, instability can be avoided. Nevertheless, in the low-SCR case, the oscillations are not sufficiently damped if R_v of the FVR model is disabled too early.

Overall, in the low-SCR condition, the AVR can suppress the post-fault oscillations and significantly enhance the post-fault transient, as shown in Fig. 14. In the higher-SCR case, the impact of the AVR reduces as the oscillation intensity diminishes. The effectiveness of the FVR model is validated in the low-SCR condition. However, this model causes adverse impacts on the GFMI's stability when it comes to a stiffer grid condition. The experimental results verify the discussions in Sections II and III.

V. Conclusions

Weak grid condition and non-ideally-tuned controls of GFMIs can lead to severe post-fault oscillations in the power network. Hence, a damping mechanism is required to suppress these oscillations, enhancing the recovery of the GFMIs from faults. The VR can be used for this purpose. The VR is only active when a fault recovery is detected and disabled during the normal operation of the GFMI. The VR can be optimally tuned to operate in a specific condition. However, due to the changes in the network topology, grid strength varies over time. This fact degrades the performance of the VR or even causes instability of the GFMI. Therefore, an adaptive VR model is necessary. This paper proposes an AVR model that can self-adjust its resistance according to the post-fault oscillation intensity to sufficiently dampen the oscillatory post-fault transient while avoiding degrading the fault recovery. The AVR model is implemented in an SRF and requires several modifications in the inner current control loop. The effectiveness of the AVR is validated in various grid strength conditions both in simulation and experiments.

References

[1] M. G. Taul, X. Wang, P. Davari, and F. Blaabjerg, "Current limiting control with enhanced dynamics of grid-forming converters during fault conditions," *IEEE Trans. Emerg. Sel. Topics Power Electron.*, vol. 8, no. 2, pp. 1062–1073, Jun. 2020.

[2] J. Rocabert, A. Luna, F. Blaabjerg, and P. Rodríguez, "Control of power converters in ac microgrids," *IEEE Trans. Power Electron.*, vol. 27, no. 11, pp. 4734–4749, Nov. 2012.

[3] J. Z. Zhou, H. Ding, S. Fan, Y. Zhang, and A. M. Gole, "Impact of short-circuit ratio and phase-locked-loop parameters on the small-signal behavior of a vsc-hvdc converter," *IEEE Trans. Power Del.*, vol. 29, no. 5, pp. 2287–2296, Oct. 2014.

[4] M. G. Taul, X. Wang, P. Davari, and F. Blaabjerg, "An overview of assessment methods for synchronization stability of grid-connected converters under severe symmetrical grid faults," *IEEE Trans. Power Electron.*, vol. 34, no. 10, pp. 9655–9670, Oct. 2019.

[5] M. C. Chandorkar, D. M. Divan, and R. Adapa, "Control of parallel connected inverters in standalone ac supply systems," *IEEE Trans. Ind. Appl.*, vol. 29, no. 1, pp. 136–143, Jan. 1993.

[6] W. Du, Z. Chen, K. P. Schneider, R. H. Lasseter, S. Pushpak Nandanoori, F. K. Tuffner, and S. Kundu, "A comparative study of two widely used grid-forming droop controls on microgrid small-signal stability," *IEEE Trans. Emerg. Sel. Topics Power Electron.*, vol. 8, no. 2, pp. 963–975, Jun. 2020.

[7] J. Driesen and K. Visscher, "Virtual synchronous generators," in *2008 IEEE Power and Energy Society General Meeting - Conversion and Delivery of Electrical Energy in the 21st Century*, Jul. 2008, pp. 1–3.

[8] X. Meng, J. Liu, and Z. Liu, "A generalized droop control for grid-supporting inverter based on comparison between traditional droop control and virtual synchronous generator control," *IEEE Trans. Power Electron.*, vol. 34, no. 6, pp. 5416–5438, Jun. 2019.

[9] L. Zhang, L. Harnefors, and H. Nee, "Power-synchronization control of grid-connected voltage-source converters," *IEEE Trans. Power Syst.*, vol. 25, no. 2, pp. 809–820, May 2010.

[10] B. B. Johnson, M. Sinha, N. G. Ainsworth, F. Dörfler, and S. V. Dhople, "Synthesizing virtual oscillators to control islanded inverters," *IEEE Trans. Power Electron.*, vol. 31, no. 8, pp. 6002–6015, Aug. 2016.

[11] D. Pan, X. Wang, F. Liu, and R. Shi, "Transient stability of voltage-source converters with grid-forming control: A design-oriented study," *IEEE Trans. Emerg. Sel. Topics Power Electron.*, vol. 8, no. 2, pp. 1019–1033, Jun. 2020.

[12] A. Tayyebi, D. Groß, A. Anta, F. Kupzog, and F. Dörfler, "Frequency stability of synchronous machines and grid-forming power converters," *IEEE Trans. Emerg. Sel. Topics Power Electron.*, vol. 8, no. 2, pp. 1004–1018, Jun. 2020.

[13] T. Qoria, F. Gruson, F. Colas, X. Kestelyn, and X. Guillaud, "Current limiting algorithms and transient stability analysis of grid-forming vscs," *Electric Power Systems Research*, vol. 189, p. 106726, Dec. 2020.

[14] N. Bottrell and T. C. Green, "Comparison of current-limiting strategies during fault ride-through of inverters to prevent latch-up and wind-up," *IEEE Trans. Power Electron.*, vol. 29, no. 7, pp. 3786–3797, Jul. 2014.

[15] K. Shi, W. Song, P. Xu, R. Liu, Z. Fang, and Y. Ji, "Low-voltage ride-through control strategy for a virtual synchronous generator based on smooth switching," *IEEE Access*, vol. 6, pp. 2703–2711, 2018.

[16] S. Huang, J. Schmall, J. Conto, J. Adams, Y. Zhang, and C. Carter, "Voltage control challenges on weak grids with high penetration of wind generation: Ercot experience," in *2012 IEEE Power and Energy Society General Meeting*, Jul. 2012, pp. 1–7.

[17] H. Mahmood, D. Michaelson, and J. Jiang, "Accurate reactive power sharing in an islanded microgrid using adaptive virtual impedances," *IEEE Trans. Power Electron.*, vol. 30, no. 3, pp. 1605–1617, Mar. 2015.

[18] A. Rodríguez-Cabero, J. Roldán-Pérez, and M. Prodanovic, "Virtual impedance design considerations for virtual synchronous machines in weak grids," *IEEE Trans. Emerg. Sel. Topics Power Electron.*, vol. 8, no. 2, pp. 1477–1489, Jun. 2020.

[19] A. D. Paquette and D. M. Divan, "Virtual impedance current limiting for inverters in microgrids with synchronous generators," *IEEE Trans. Ind Appl.*, vol. 51, no. 2, pp. 1630–1638, Mar. 2015.

[20] G. Denis, T. Prevost, M. S. Debry, F. Xavier, X. Guillaud, and A. Menze, "The migrate project: The challenges of operating a transmission grid with only inverter-based generation. a grid-forming control improvement with transient current-limiting control," *IET Renewable Power Generation*, vol. 12, pp. 523–529, Apr. 2018.

[21] X. Lin, Y. Zheng, Z. Liang, and Y. Kang, "The suppression of voltage overshoot and oscillation during the fast recovery process from load short-circuit fault for three-phase stand-alone inverter," *IEEE Trans. Emerg. Sel. Topics Power Electron.*, vol. 9, no. 1, pp. 858–871, Feb. 2021.

[22] L. Huang, H. Xin, Z. Wang, L. Zhang, K. Wu, and J. Hu, "Transient stability analysis and control design of droop-controlled voltage source converters considering current limitation," *IEEE Trans. Smart Grid*, vol. 10, no. 1, pp. 578–591, Jan. 2019.

[23] S. D'Arco, J. A. Suul, and O. B. Fosso, "Automatic tuning of cascaded controllers for power converters using eigenvalue parametric sensitivities," *IEEE Trans. Ind Appl.*, vol. 51, no. 2, pp. 1743–1753, Mar. 2015.

[24] B. Bahrani, "Advanced control strategies for voltage source converters in microgrids and traction networks," Ph.D. dissertation, EPFL, Lausanne, 2012.

[25] T. Qoria, F. Gruson, F. Colas, G. Denis, T. Prevost, and X. Guillaud, "Critical clearing time determination and enhancement of grid-forming converters embedding virtual impedance as current limitation algorithm," *IEEE Trans. Emerg. Sel. Topics Power Electron.*, vol. 8, no. 2, pp. 1050–1061, Jun. 2020.

[26] J. Liu, Y. Miura, and T. Ise, "Comparison of Dynamic Characteristics Between Virtual Synchronous Generator and Droop Control in Inverter-Based Distributed Generators," *IEEE Trans. Power Electron.*, vol. 31, no. 5, pp. 3600–3611, 2016.

[27] F. Welck, D. Duckwitz, and C. Gloeckler, "Influence of virtual impedance on short circuit performance of virtual synchronous machines in the 9-bus system," in *Proc. Conf. Sustain. Energy Supply Energy Storage Syst. (NEIS).* VDE, Sep. 2017, pp. 1–7.

[28] E. Afshari, G. R. Moradi, R. Rahimi, B. Farhangi, Y. Yang, F. Blaabjerg, and S. Farhangi, "Control strategy for three-phase grid-connected pv inverters enabling current limitation under unbalanced faults," *IEEE Trans. Ind. Electron.*, vol. 64, no. 11, pp. 8908–8918, Nov. 2017.

[29] K. J. Astrom and T. Hagglund, *PID Controllers: Theory, Design, and Tuning*, 2nd ed. Research Triangle Park, NC, USA: Intl. Society for Measurement and Con, Jan. 1995.

[30] X. Wang and F. Blaabjerg, "Harmonic stability in power electronic-based power systems: Concept, modeling, and analysis," *IEEE Trans. Smart Grid*, vol. 10, no. 3, pp. 2858–2870, May. 2019.

[31] B. Mahamedi, M. Eskandari, J. E. Fletcher, and J. Zhu, "Sequence-based control strategy with current limiting for the fault ride-through of inverter-interfaced distributed generators," *IEEE Trans. Sustain. Energy*, vol. 11, no. 1, pp. 165–174, Jan. 2020.

[32] W. Du, Q. Fu, and H. F. Wang, "Power System Small-Signal Angular Stability Affected by Virtual Synchronous Generators," *IEEE Trans. Power Syst.*, vol. 34, no. 4, pp. 3209–3219, 2019.

Frede Blaabjerg (S'86–M'88–SM'97–F'03) was with ABB-Scandia, Randers, Denmark, from 1987 to 1988. From 1988 to 1992, he got the PhD degree in Electrical Engineering at Aalborg University in 1995. He became an Assistant Professor in 1992, an Associate Professor in 1996, and a Full Professor of power electronics and drives in 1998. From 2017 he became a Villum Investigator. He is honoris causa at University Politehnica Timisoara (UPT), Romania and Tallinn Technical University (TTU) in Estonia.

His current research interests include power electronics and its applications such as in wind turbines, PV systems, reliability, harmonics and adjustable speed drives. He has published more than 600 journal papers in the fields of power electronics and its applications. He is the co-author of four monographs and editor of ten books in power electronics and its applications.

He has received 33 IEEE Prize Paper Awards, the IEEE PELS Distinguished Service Award in 2009, the EPE-PEMC Council Award in 2010, the IEEE William E. Newell Power Electronics Award 2014, the Villum Kann Rasmussen Research Award 2014, the Global Energy Prize in 2019 and the 2020 IEEE Edison Medal. He was the Editor-in-Chief of the IEEE TRANSACTIONS ON POWER ELECTRONICS from 2006 to 2012. He has been Distinguished Lecturer for the IEEE Power Electronics Society from 2005 to 2007 and for the IEEE Industry Applications Society from 2010 to 2011 as well as 2017 to 2018. In 2019-2020 he served as a President of IEEE Power Electronics Society. He has been Vice-President of the Danish Academy of Technical Sciences. He is nominated in 2014-2020 by Thomson Reuters to be between the most 250 cited researchers in Engineering in the world.
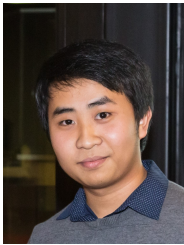
Si Phu Me (S'19) received the B.E. degree in electrical and computer systems engineering from Monash University, Victoria, Australia, in 2019. He is currently pursuing the Ph.D. degree in power electronic engineering at Monash University.

His research interests include control and stability analysis of power electronic converters.

Behrooz Bahrani (M'13–SM'19) received the B.Sc. degree from Sharif University of Technology, Tehran, Iran, the M.Sc. degree from the University of Toronto, Toronto, ON, Canada, and the PhD degree from the Ecole Polytechnique Federale de Lausanne (EPFL), Lausanne, Switzerland, all in electrical engineering, in 2006, 2008, and 2012, respectively. From September 2012 to September 2015, he was a Postdoctoral Fellow at EPFL, Purdue University, West Lafayette, IN, USA, Georgia Institute of Technology, Atlanta, GA, USA, and the Technical University of Munich, Munich, Germany. Since 2015, he has been with Monash University, where currently, he is a Senior Lecturer and the Director of the Grid Innovation Hub. His research interests include control of power electronic converters, their applications in power systems, and grid integration of renewable energy resources.

Sasan Zabihi (S'09 M'11 SM'20) received his Ph.D. degree in Power Electronics control and applications from QUT, Australia in 2011. He then served as a lecturer at QUT up to 2012. Prior to joining QUT in 2008, he was a senior development engineer with multiple energy research institutes, with a focus on control and topology design for power conversion and custom power devices. Since 2013, he has been an R&D specialist with ABB Australia (now HITACHI ABB Power Grids), in their global CoC for Microgrid, and distributed generation, developing power converters, and associated controls for Microgrids, Energy Storage and Renewable applications, and facilitating their integration into Power Systems. His focus lately has been shifted to addressing transient stability and system strength challenges ahead of our future Grids with ever-increasing penetration of renewables. He is an active member of several CIGRE working groups and IEEE task forces. Dr Zabihi is currently an Adjunct Associate Professor at Monash University.